nature geoscience

SUPPLEMENTARY INFORMATION

DOI: 10.1038/NGEO955

External forcing as a metronome for Atlantic multidecadal variability

Odd Helge Otterå*, Mats Bentsen, Helge Drange and Lingling Suo

*To whom correspondence should be addressed; E-mail: Odd.Ottera@uni.no.

S.1 Model description.

The climate model used in this study is an updated version of the Bergen Climate Model (BCM) [1], a global coupled atmosphere−sea-ice−ocean general circulation model (GCM). The atmosphere component is the spectral atmospheric GCM ARPEGE [2]. In the present study, ARPEGE is run with a truncation at wave number 63 (T_L63), and a time step of 1800 s. All the physics and the treatment of model nonlinear terms require spectral transforms to a Gaussian grid. This grid (about 2.8° resolution in longitude and latitude) is reduced near the poles to give an approximately uniform horizontal resolution (on the target sphere) and to save computational time. The vertical hybrid coordinate follows the topography in the lower troposphere, but becomes gradually parallel to pressure surfaces with increasing height. In this study, a total of 31 vertical levels are employed, ranging from the surface to 0.01 hPa. The physical parametrization is divided into several explicit schemes, each calculating the flux of mass, energy and/or momentum due to a specific physical process [1].

The ocean component is MICOM [3, 4], a global isopycnic coordinate ocean GCM. In the version of MICOM used in this study, several important aspects deviate from the original model and the one used in the original version of BCM [1]. Firstly, MICOM now uses a reference pres-

DOI: 10.1038/NGEO955

sure of 2000 db whereas previous versions used a reference pressure of 0 db. This will reduce the non-neutrality of the isopycnals in the world ocean compared to having the reference pressure at the surface [5]. Secondly, the conservation properties of tracers (i.e. salinity, potential temperature and passive tracers) have been greatly improved compared to earlier versions. The use of incremental remapping [6] for the advection of tracers has contributed to this. Thirdly, shear instability and gravity current mixing have been incorporated by adding a Richardson number dependent diffusivity to the background diffusivity. This has greatly improved the water mass characteristics downstream of overflow regions. Finally, the pressure gradient formulation used in the new version of MICOM is based on the formulation of Janic [7], where the pressure gradient is expressed as a gradient of the geopotential on a pressure surface. This allows a more accurate representation of density in the pressure gradient formulation compare to earlier versions of MICOM. With the exception of the equatorial region, the ocean grid is almost regular with horizontal grid resolution of approximately $2.4^\circ \times 2.4^\circ$. In order to better resolve the dynamics near the equator, the horizontal resolution in the meridional direction is gradually increased to 0.8° along the equator. The model has a stack of 34 isopycnic layers in the vertical, with potential densities ranging from 1030.119 to 1037.800 kg m^{-3}, and a non-isopycnic surface mixed layer on top providing the linkage between the atmospheric forcing and the ocean interior.

The processes that transfer water between the mixed layer and isopycnic layers are entrainment/detrainment due to mixed layer deepening/retreat, respectively, and convective adjustment when the mixed layer and isopycnic layers are hydrostatically unstable. The mixed layer depth is found by a turbulent kinetic energy balance of a one-dimensional mixed layer of the type described by Krauss and Turner [8]. However, the formulation by Gaspar [9] is used in this version of MICOM. Entrainment into and detrainment from the mixed layer follow largely Bleck et al. [4]. The entrainment process is straightforward to incorporate in a physical and robust

manner in an isopycnic model with a bulk mixed layer since the mixed layer does not have any density constraints. Detrainment is more challenging since water detrained from the mixed layer should match the potential density of the receiving isopycnic layer. We have slightly modified the original Bleck et al. detrainment approach to better preserve water mass properties at high latitudes by more faithfully incorporating the impact of salinity on density. When the mixed layer is denser than mass containing isopycnic layers, the mixed layer water is split into a plume fraction with a density matching the first denser isopycnic layer and a remaining fraction that is hydrostatically stable. Temperature and salinity of the plume fraction is constructed by assuming that the contribution of temperature and salinity tendencies in changing the mixed layer density will prevail. The plume fraction inflates the layer with matching density and water from the first unstable isopycnic layer replaces the plume fraction in the mixed layer, thus keeping the mixed layer volume constant during the convective adjustment process.

The sea-ice model is GELATO, a dynamic-thermodynamic sea-ice model that include multiple ice categories [10]. All equations in GELATO are solved on an Arakawa B-grid which shares its grid points with the C-grid of the ocean model. A linear interpolation between the two grids is performed internally by the sea-ice model. The OASIS (version 2) coupler [11, 12] has been used to couple the atmosphere and ocean models.

The coupled model is run without any form of flux adjustments. A global SST drift of about 0.1°C per century [13] is evident during the first few centuries of the model integrations. The model drift is particular evident in the Southern Ocean, but can also be seen to some degree in the sub-polar region. For the last 400 years only minor drifts are found in the SST.

S.2 Ocean response to NAO interannual variability

NAO is the dominant mode of atmospheric variability in the North Atlantic sector. Basin scale changes in the atmospheric forcing significantly affect the properties and circulation of the

DOI: 10.1038/NGEO955

ocean. Previous studies of interannual variability in ocean hindcast simulations using MICOM have focused on the role of the sub-polar gyre for the AMOC [14, 15]. Here we briefly examine the ocean response to interannual variations in the atmospheric forcing associated with the NAO in BCM, and compare it to observations. In Fig. S4A, we show the regression coefficients between observed NOAA SST data [16] for the last 50 years and the observed NAO index [17]. The spatial pattern is characterized by positive temperature anomalies between about 30°N and 45°N in the western North Atlantic, and negative temperature anomalies in the sub-polar gyre region (north of 45°N). In addition to the North Atlantic SST dipole, negative temperature anomalies are apparent in the TNA. This SST response pattern is often referred to as the NAO SST tripole pattern. The simulated SST tripole pattern in CTL600 is in qualitative agreement with the observations (Fig. S4B). However, the model tend to underestimate the cooling signal in the sub-polar gyre region, and the cold lobe in the TNA is narrower than in the observations.

Changes in the local air-sea heat fluxes are likely the cause for the observed SST anomaly pattern. In Fig. S4C the observed winter season (DJF) averaged total heat flux anomalies, calculated from NCEP/NCAR reanalysis data [18], are regressed on the observed NAO index. The corresponding heat flux anomalies in BCM are shown in Fig. S4D. In the observations as well as in the model there is a good spatial correspondence of the air-sea flux anomalies with the SST anomalies as well as their corresponding magnitude. On interannual time scales, it therefore seems like the upper ocean temperature response can be rationalized in terms of a simple local mixed layer heat budget calculation [19, 20].

Variations in the NAO index and associated wind fields imply strong changes in surface air-sea flux fields of heat and momentum. These changes impact both the local thermodynamic response of the mixed layer and the large-scale circulation field. In Fig. S4E and Fig. S4F, we show the winter season (DJF) averaged wind stress anomalies regressed on the observed and simulated NAO indices, respectively. The overall pattern shows enhanced and northerly

displaced westerlies north of 45°N, as well as slightly enhanced trade winds between 10°N and 30°N. Notice also the increased advection of cold Arctic air masses within the Labrador Sea, as inferred from the regression map of wind stress. The simulated westerlies in CTL600 are generally more zonal than the observations. This is a general problem in GCMs, BCM included [13].

S.3 Simulated AMOC and Labrador Sea mixing

It is well established that there is a clear correspondence between formation of intermediate to deep waters in the North Atlantic and the AMOC [21, 22]. The deep-water formation in BCM takes place both to the north and to the south of the Greenland-Scotland ridge. Convectively active regions, as indicated by large mixed layer (ML) depths (Fig. S5A), can be seen in the central Greenland Sea gyre and south of the Greenland-Scotland Ridge in the Irminger and Labrador Seas (the spatial pattern is very similar for EXT600). We define the mixing regions in the model as the areas where the March ML thickness exceeds 1200 m at least once during CTL600 and EXT600 (Fig. S5B). In Fig. S5C, the monthly mean ML depths for the Labrador, Irminger and GIN Seas are shown for CTL600. The ML penetrates deepest in the Labrador Sea with a ML thickness of about 700 m, whereas the ML depth in the GIN Sea is shallower with a maximum ML thickness of about 400 m. The relation between the ML density in the Labrador Sea mixing region and the AMOC is investigated by calculating the cross-correlations between the respective low-pass filtered time series (Fig. S5D). The density in the Labrador Sea mixing region leads the AMOC by several years, suggesting that density fluctuations precondition the water column and eventually modulate the convection strength.

DOI: 10.1038/NGEO955

S.4 Power spectra of AMO, AMOC and NAO

The power spectra of the AMO and AMOC indices in CTL600 and EXT600 are shown in Fig. S6A and Fig. S6B, respectively. It follows that most of the energy is found on decadal time scales. Furthermore, the power spectra confirm that the AMO and AMOC in EXT600 have significantly more power in the 60-100 year band than in CTL600. In EXT600 there is also a shift towards higher AMO amplitudes, as indicated by the histograms in Fig. S6C. It thus appear as if the external forcing is able to significant shift the AMO characteristics. Finally, it should also be noted that the power spectra for the simulated NAO indices for CTL600 and EXT600 are approximately white (Fig. S6D). Also, there is no significant change in the NAO variance at lower frequencies when the external forcing is included.

References

[1] Furevik, T. *et al.* Description and validation of the Bergen Climate Model: ARPEGE coupled with MICOM. *Clim. Dyn.* **21**, 27–51 (2003).

[2] Déqué, M., Dreveton, C., Braun, A. & Cariolle, D. The ARPEGE/IFS atmosphere model: A contribution to the French community climate modelling. *Clim. Dyn.* **10**, 249–266 (1994).

[3] Bleck, R. & Smith, L. T. A wind-driven isopycnic coordinate model of the North and Equatorial Atlantic Ocean. 1. Model development and supporting experiments. *J. Geophys. Res.* **95**, 3273–3285 (1990).

[4] Bleck, R., Rooth, C., Hu, D. & Smith, L. T. Salinity-driven thermocline transients in a wind- and thermohaline-forced isopycnic coordinate model of the North Atlantic. *J. Phys. Oceanogr.* **22**, 1486–1505 (1992).

[5] McDougall, T. J. & Jackett, D. R. An assessment of orthobaric density in the global ocean. *J. Phys. Oceanogr.* **35**, 2054–2075 (2005).

[6] Dukowicz, J. K. & Baumgardner, J. R. Incremental remapping as a transport/advection algorithm. *J. Comput. Phys.* **160**, 318–335 (2000).

[7] Janic, Z. I. Pressure gradient force and advection scheme used for forecasting with steep and small scale topography. *Beitr. Phys. Atmos.* **50**, 186–199 (1977).

[8] Kraus, E. B. & Turner, J. S. A one-dimensional model of the seasonal thermocline. Part II: The general theory and its consequences. *Tellus* **19**, 98–105 (1967).

[9] Gaspar, P. Modelling the seasonal cycle of the upper ocean. *J. Phys. Oceanogr.* **18**, 161–180 (1988).

DOI: 10.1038/NGEO955

[10] Salas-Melia, D. A global coupled sea ice-ocean model. *Ocean Mod.* **4**, 137–172 (2002).

[11] Terray, L. & Thual, O. Oasis: le couplage océan-atmosphére. *La Météorologie* **10**, 50–61 (1995).

[12] Terray, L. *et al.* Climatology and interannual variability simulated by the ARPEGE-OPA model. *Clim. Dyn.* **11**, 487–505 (1995).

[13] Otterå, O. H., Bentsen, M., Bethke, I. & Kvamstø, N. G. Simulated pre-industrial climate in Bergen Climate Model (version 2): Model description and large-scale circulation features. *Geosci. Mod. Dev.* **2**, 197–212 (2009).

[14] Hátún, H., Sandø, A. B., Drange, H., Hansen, B. & Valdimarsson, H. Influence of the Atlantic subpolar gyre on the thermohaline circulation. *Science* **309**, 1841–1844 (2005).

[15] Lohmann, K., Drange, H. & Bentsen, M. Response of the North Atlantic subpolar gyre to persistent North Atlantic Oscillation like forcing. *Clim. Dyn.* **32**, 273–285 (2008).

[16] Smith, T. M., Reynolds, R. W., Peterson, T. C. & Lawrimore, J. Improvements to NOAA's historical merged land-ocean surface temperature analysis (1880-2006). *J. Clim.* **21**, 2283–2296 (2008).

[17] Hurrell, J. W. Decadal trends in the North Atlantic Oscillation: Regional temperatures and precipation. *Science* **269**, 676–679 (1995).

[18] Kalnay, E. *et al.* The NCEP/NCAR 40-year reanalysis project. *Bull. Amer. Met. Soc.* **77(3)**, 437–471 (1996).

[19] Battisti, D. S., Bhatt, U. S. & Alexander, M. A. A modeling study of the interannual variability in the wintertime North Atlantic Ocean. *J. Clim.* **8**, 3067–3083 (1995).

[20] Seager, R. *et al.* Causes of Atlantic Ocean climate variability between 1958 and 1998. *J. Clim.* **13**, 2845–2862 (2000).

[21] Eden, C. & Jung, T. North Atlantic interdecadal variability: Oceanic response to the North Atlantic Oscillation (1865-1997). *J. Clim.* **14**, 676–691 (2001).

[22] Bentsen, M., Drange, H., Furevik, T. & Zhou, T. Simulated variability of the Atlantic meridional overturning circulation. *Clim. Dyn.* **22**, 701–720 (2004).

[23] Boucher, O. & Pham, M. History of sulfate aerosol radiative forcings. *Geophys. Res. Lett.* **29(9)**, 1308 (2002).

[24] Crowley, T. J., Baum, S. K., Kim, K.-Y., Hegerl, G. C. & Hyde, W. T. Modeling ocean heat content changes during the last millennium. *Geophys. Res. Lett.* **30**, 1932 (2003).

[25] Krakauer, N. Y. & Randerson, J. T. Do volcanic eruptions enhance or diminish net primary production? Evidence from tree rings. *Glob. Biogeoch. Cycles* **17**, 1118 (2003).

DOI: 10.1038/NGEO955

Figure legends

Fig. S1. Annual mean tropospheric sulphate aerosol burden (mg S m^{-2}) for the years 1850, 1900, 1920, 1930, 1940, 1950, 1960, 1970, 1980 and 1990 [23].

Fig. S2. Annual concentrations of the three most important well-mixed greenhouse gases used to force the model over the last 150 years. (A) CO_2, (B) CH_4 and (C) N_2O.

Fig. S3. (A) Simulated spatial pattern associated with EOF3 (°C per SD) in CTL600 obtained by regressing the low-passed filtered global SST data on a standardized version of the associated third principal component (PC3). Also shown is the variance explained. (B) Simulated standardized AMO and AMOC indices in CTL600 together with the PC3 of low-passed filtered SST. (C) Cross-correlations of the simulated AMO and PC3 with the AMOC in CTL600. Positive lags mean that the AMOC is leading.

Fig. S4. (A) Observed spatial SST pattern obtained by regressing the observed unfiltered winter (DJF) NOAA SST data [16] on a standardized (unit variance) version of the observed winter (DJF) NAO index [17]. (B) Simulated spatial SST pattern obtained by regressing the unfiltered winter (DJF) SST data in CTL600 on a standardized (unit variance) version of the simulated NAO index. Here the NAO index is defined as the principal component associated to the leading EOF of winter (DJF) sea level pressure north of 20°N. (C) Observed spatial pattern of total heat flux (positive to the ocean) obtained by regressing unfiltered winter (DJF) total heat flux NCEP-NCAR reanalysis data [18] on a standardized (unit variance) version of the observed winter (DJF) NAO index. (D) Same as (B), but for the total heat flux (positive to the ocean). (E) Same as (C), but for the NCEP-NCAR momentum flux (wind-stress). (F) Same as (B), but for the momentum flux (wind-stress).

Fig. S5 (A) Average mixed layer depth in March for CTL600 in the northern North Atlantic. (B) Mixing regions in the model. The shading represents the areas where the March mixed layer depth exceeds 1200 m at least once in CTL600 and EXT600. (C) The annual cycle of the mixed layer depth in the mixing regions shown in (B). (D) Cross-correlations of the low-pass filtered AMOC-index with the simulated Labrador Sea annual mean density for CTL600 and EXT600. Statistical significance at the 95% confidence interval is indicated by the grey shading. Positive lags mean that the AMOC is leading.

Fig. S6. (A) Power spectra of the unfiltered AMO for CTL600 (black) and EXT600 (blue) calculated using a multi-taper method (MTM). Statistical significance at the 95% confidence interval (relative to the spectrum of a fitted AR1-process) is indicated by the dashed lines. The grey shaded region indicate the frequency band with periods between 60 and 100 years. (B) Same as (A), but for the AMOC index. (C) Histograms of AMO for CTL600 (black) and for EXT600 (blue). (D) Same as (A) but for the NAO index.

Fig. S7. Simulated leading EOF of winter (DJF) sea level pressure anomalies north of 20°N in CTL600 (top) and EXT600 (bottom) together with the explained variance.

DOI: 10.1038/NGEO955

Table

Table S1: The years and estimated radiative forcings of volcanic eruptions based on the Crowley *et al.* [24] forcing data set. Also shown are the possible responsible historical eruptions.

	Eruption Description			
Year	Name	Latitude	W m^{-2}	VEI[a]
1453	Kuwae	16.8S	-4.2	6
1460	Unknown		-1.3	
1586	Kelut	7.9S	-1.3	5
1600	Huaynaputina	16.6S	-1.9	6
1620	Unknown		-1.1	
1641	Parker	6.1N	-1.7	5
1674	Gamnokara	1.4N	-1.5	5
1680	Unknown		-1.1	
1693	Serusa	6.3S	-1.1	4
1809	Unknown		-2.9	
1815	Tambora	8.3S	-5.6	7
1831	Babuyan Claro	19.5N	-1.3	4
1835	Cosiguina	13.0N	-1.4	5
1883	Krakatau	6.1S	-2.6	6
1902	Santa Maria	14.8N	-1.3	6
1963	Agung	8.3S	-1.9	4
1982	El Chicon	17.4N	-2.1	5
1991	Pinatubo	15.1N	-3.3	6

Note that in many cases the most important contributing eruption is uncertain or unknown.
[a]VEI = Volcanic Explosivity Index [25]; 4 is "large"; 5 and higher "very large".

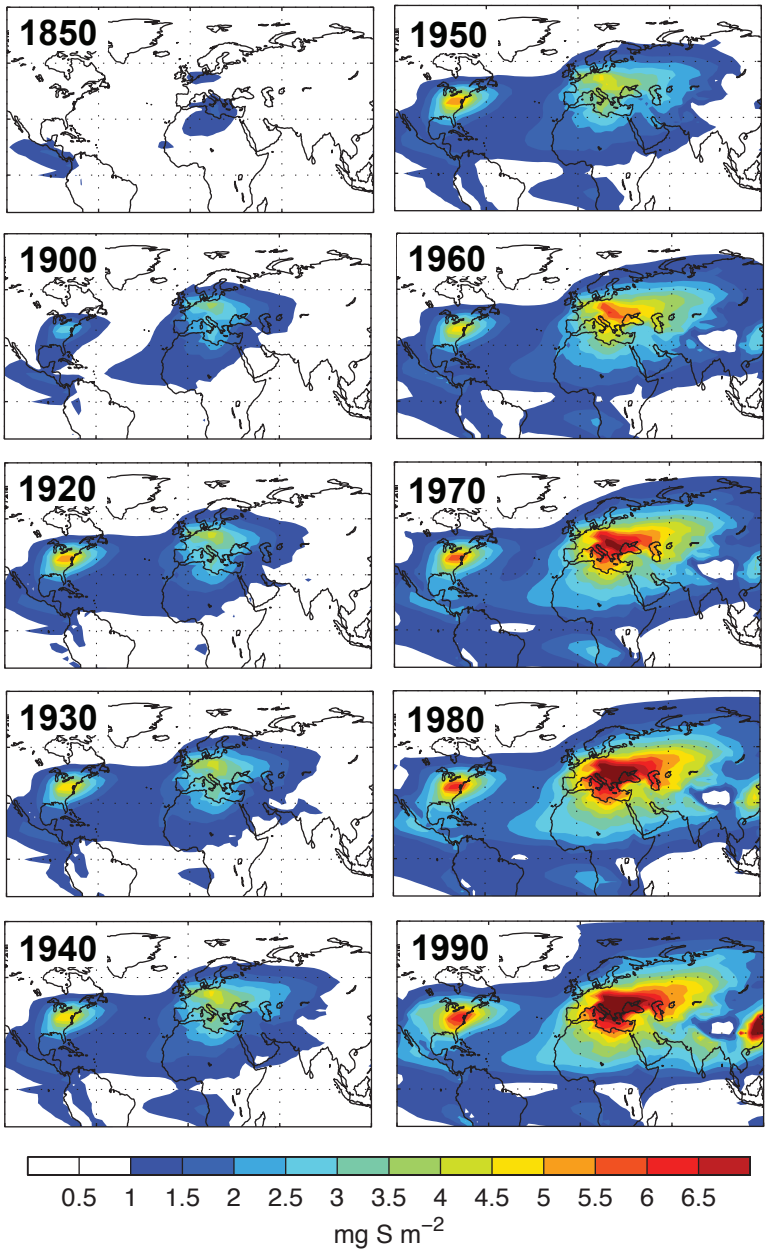
1850
1950
1900
1960
1920
1970
1930
1980
1940
1990
0.5 1 1.5 2 2.5 3 3.5 4 4.5 5 5.5 6 6.5
mg S m^{-2}

DOI: 10.1038/NGEO955

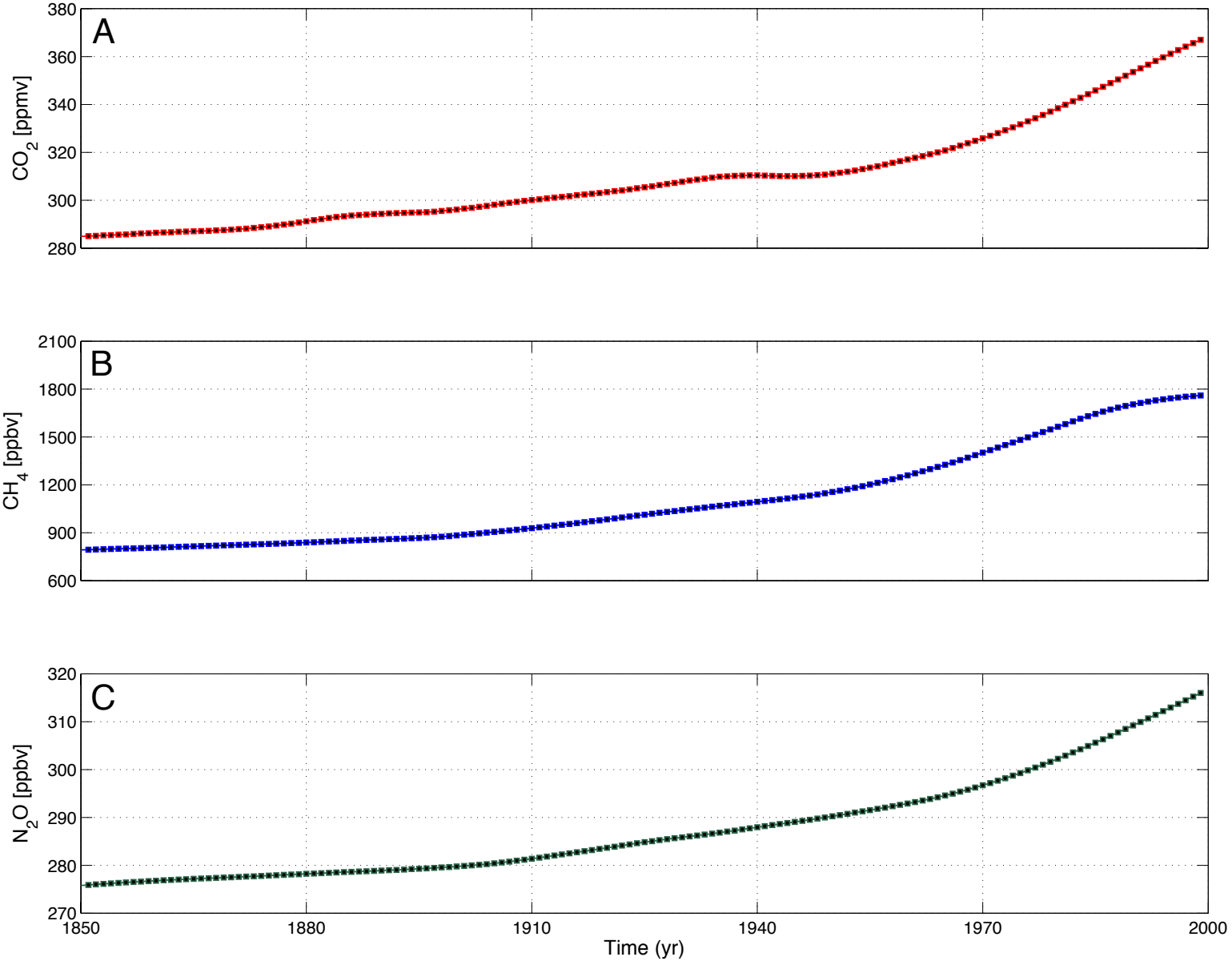

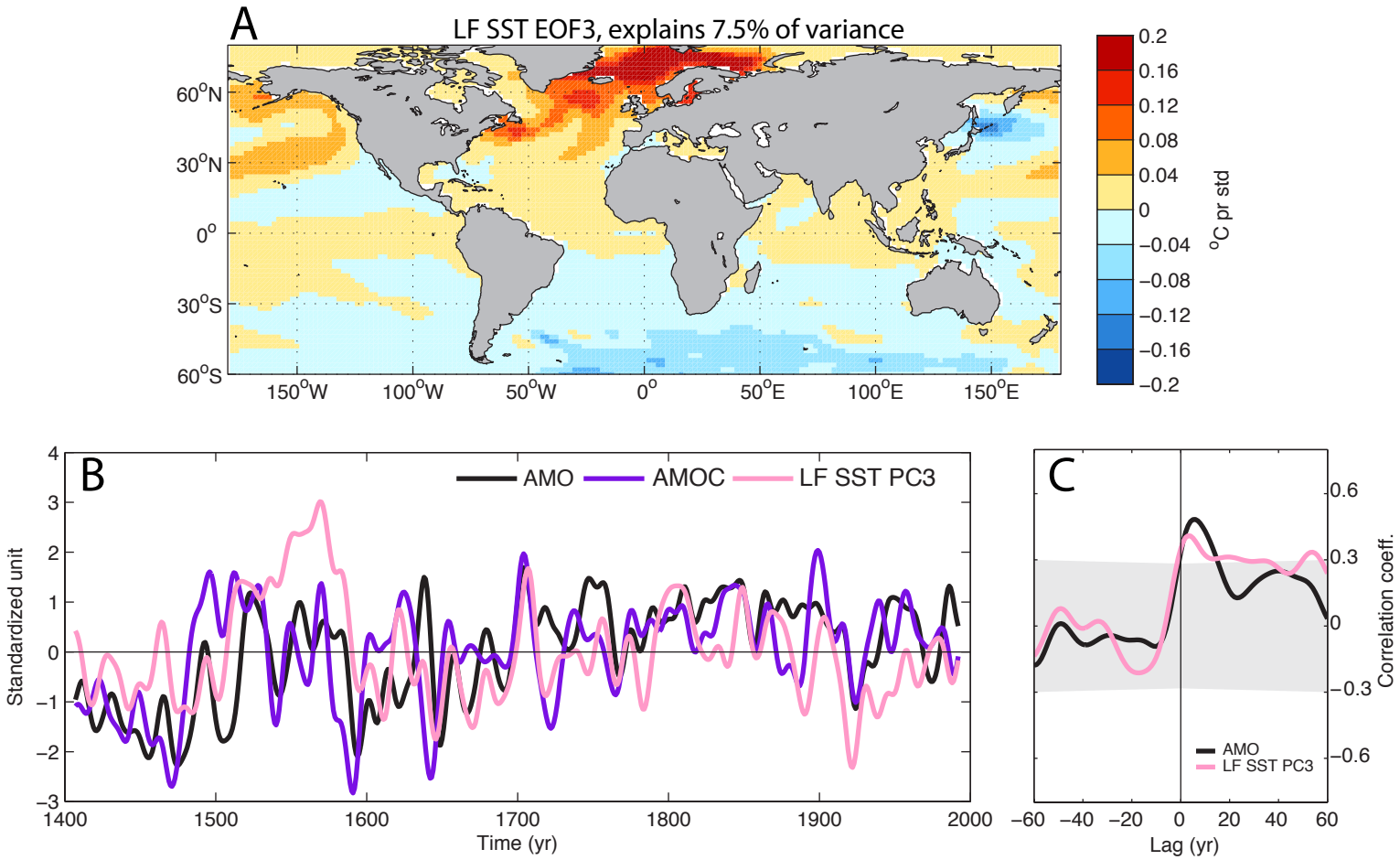
A
LF SST EOF3, explains 7.5% of variance
60°N
30°N
0°
30°S
60°S
150°W
100°W
50°W
0°
50°E
100°E
150°E
0.2
0.16
0.12
0.08
0.04
0
−0.04
−0.08
−0.12
−0.16
−0.2
°C pr std
B
AMO
AMOC
LF SST PC3
Standardized unit
Time (yr)
C
AMO
LF SST PC3
Correlation coeff.
Lag (yr)

DOI: 10.1038/NGEO955

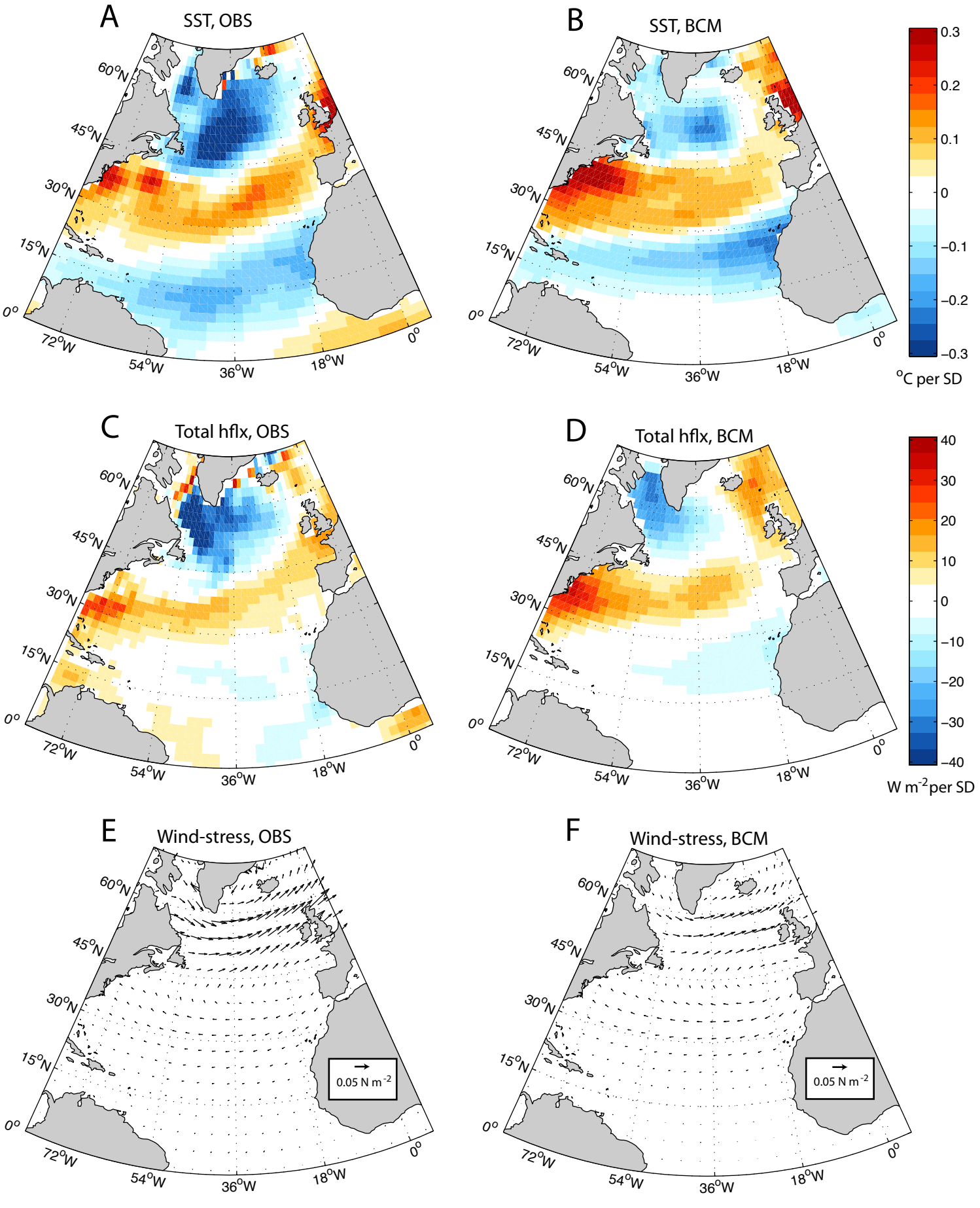

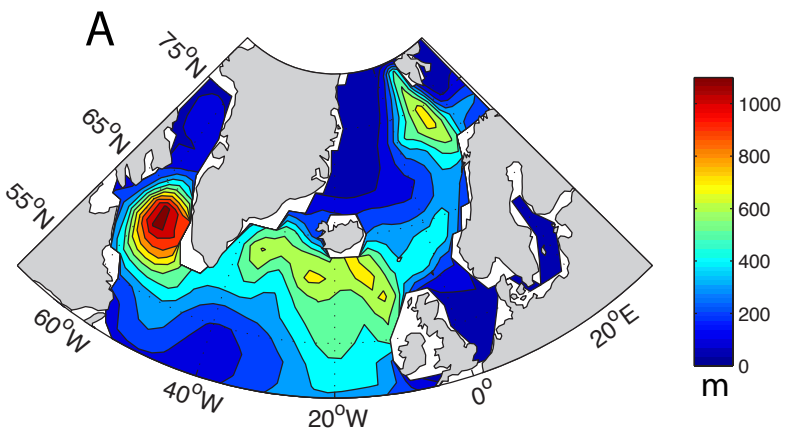
A
75°N
65°N
55°N
60°W
40°W
20°W
0°
20°E
1000
800
600
400
200
0
m

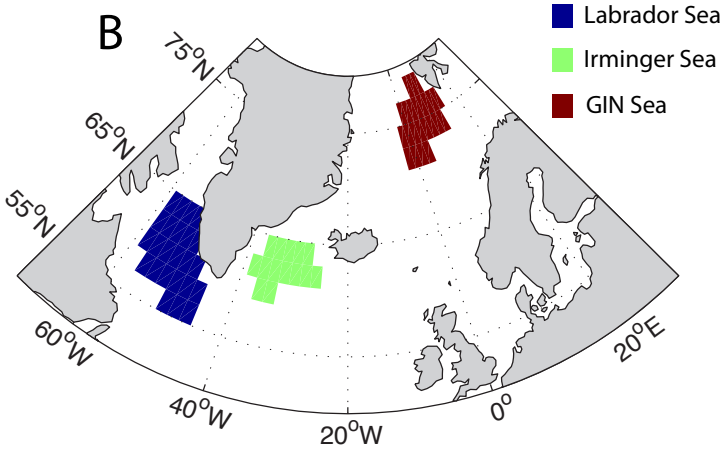
B
Labrador Sea
Irminger Sea
GIN Sea
75°N
65°N
55°N
60°W
40°W
20°W
0°
20°E

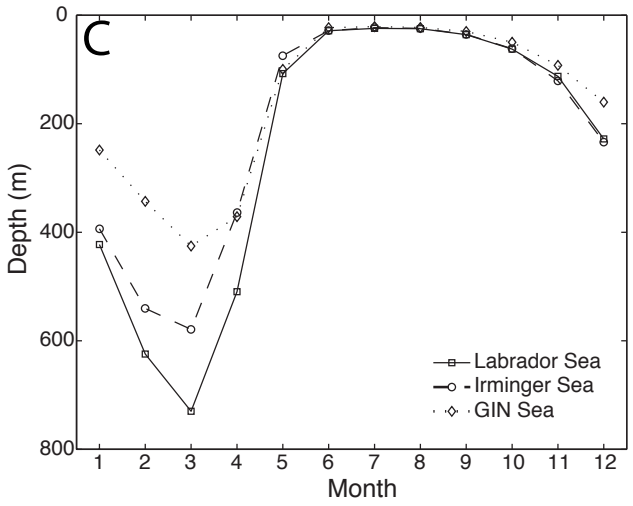
C
Depth (m)
Month
Labrador Sea
Irminger Sea
GIN Sea

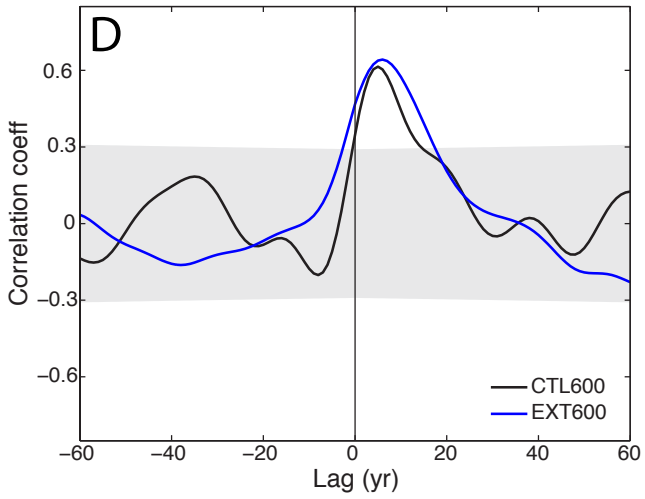
D
Correlation coeff
Lag (yr)
CTL600
EXT600

DOI: 10.1038/NGEO955

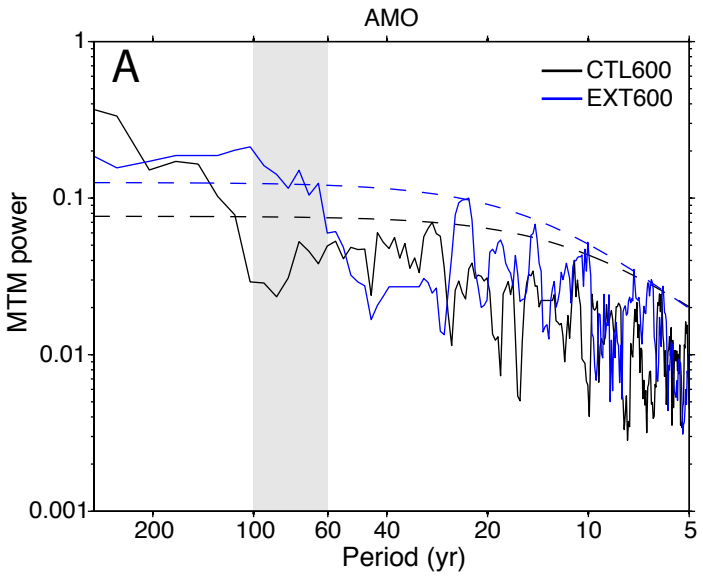

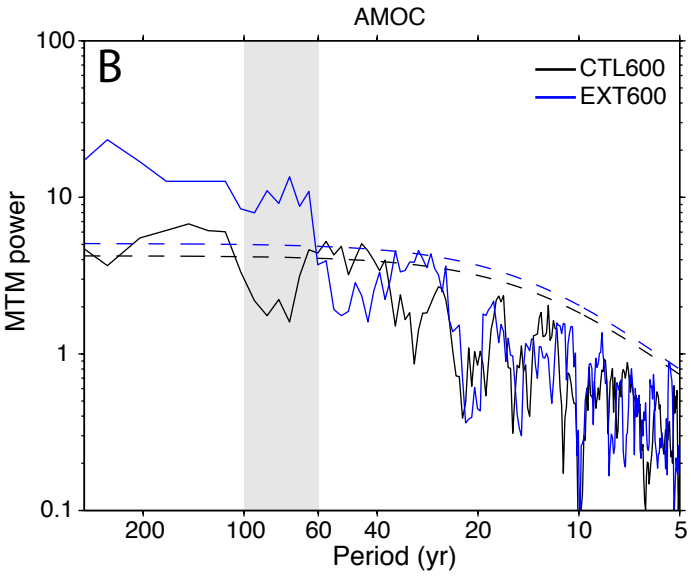

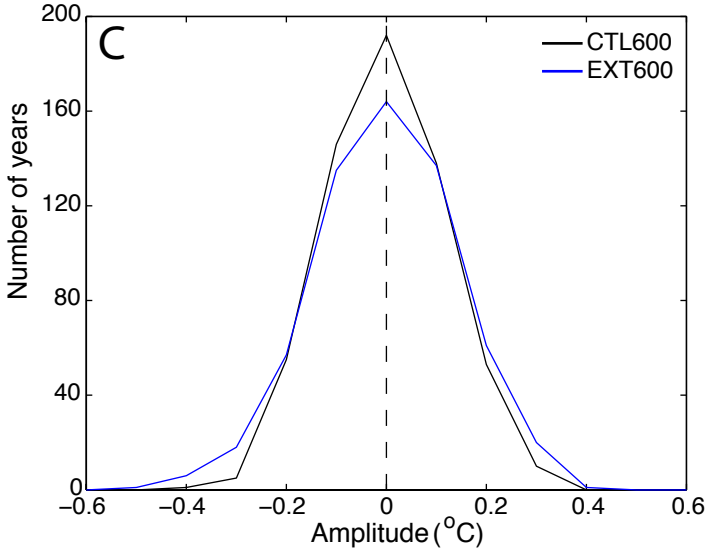

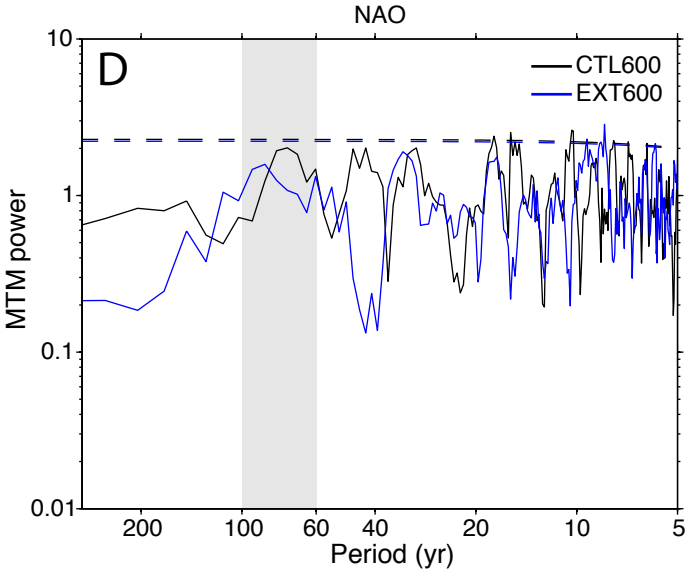

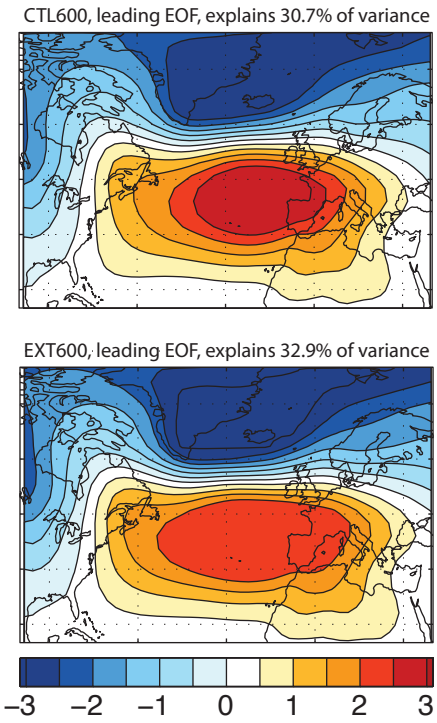
CTL600, leading EOF, explains 30.7% of variance
EXT600, leading EOF, explains 32.9% of variance
–3
–2
–1
0
1
2
3